Miniature laser powder bed fusion system for *in situ* synchrotron x-ray micro-computed tomography experiments at the European Synchrotron Radiation Facility

Pierre Lhuissier,[1,a] Louis Hébrard,[1,2] Xavier Bataillon,[1] Pierre Lapouge,[2] Frédéric Coste,[2] Patrice Peyre,[2] Elodie Boller,[3] Jean-Jacques Blandin,[1] Luc Salvo,[1] and Guilhem Martin[1,a]

AFFILIATIONS

[1] University of Grenoble Alpes, CNRS, Grenoble INP, SIMaP, F-38000 Grenoble, France

[2] Ecole Nationale Supérieure des Arts et Métiers, Laboratoire de Procédés et Ingénierie en Mécanique des Matériaux PIMM, UMR 8006 CNRS, 151, Boulevard de l'Hôpital, 75013 Paris, France

[3] ESRF-The European Synchrotron, CS40220, 38043 Grenoble Cedex 9, France

Note: Paper published as part of the special topic on Operando systems for synchrotron studies of additive manufacturing processes.

[a] **Authors to whom correspondence should be addressed:** pierre.lhuissier@simap.grenoble-inp.fr and guilhem.martin@simap.grenoble-inp.fr

ABSTRACT

We describe our miniature laser powder bed fusion (L-PBF) system for *in situ* synchrotron x-ray micro-computed tomography (XCT) at the European Synchrotron Radiation Facility. This replicator was designed to extend the characterization of L-PBF to 3D. This instrument fills in a technical gap because the existing replicators were mostly designed to shed light on the dynamic mechanisms involved in molten pool formation but, therefore, suffered from a lack of 3D information. Technical details regarding the setup and beamline integration are given. Experimental validations via post-mortem XCT scans and *in situ* scans acquired during experiments conducted at the BM05 beamline of the European Synchrotron Radiation Facility are provided. Based on a few illustrative examples, we show that such a replicator opens the path to collect key 3D information that to date could not be available. Our miniature instrument complements the other replicators developed in the world by other research groups that enable *operando* x-ray imaging (radiography) and *operando* x-ray diffraction.

I. INTRODUCTION

Among Additive Manufacturing (AM) processes for metals, laser powder bed fusion (L-PBF) is certainly the most widely used worldwide. It allows sophisticated geometries such as lattice structures or topologically optimized components to be produced.

Analyses of the laser-melt pool-powder bed interactions have recently received great attention because the molten pool stability is often considered as the pathway to building defect-free objects. Process instabilities including spattering or keyhole formation often lead to defects that can drastically reduce the mechanical performances of components fabricated by AM, particularly fatigue properties. Thus, much research effort has been made to provide a fundamental understanding of the mechanisms leading to defect formation in additively manufactured objects. High-speed optical cameras were first used for *in situ* process monitoring to estimate the density of spatters,[1–5] but this approach suffers from a major limitation since only the top surface can be observed. This limitation was recently overcome with the development of different L-PBF replicators[6–10] allowing time-resolved x-ray images to be collected during 3D printing. MHz-frame rate x-ray radiography has recently enabled to shed light on the fundamental mechanisms involved in the melt pool dynamics while melting a single track.[6,9–15] Different materials, such as Ti-alloys,[7,9,15,16] Fe-alloys,[11,13,14] Ni-alloys,[10]

and also Al-alloys,[8,11,12,15] have been characterized using such an approach. Even more recently, L-PBF replicators offering the possibility to monitor the process using x-ray diffraction to collect information regarding phase transitions were also developed.[9,17] Such *operando* approaches were eventually complemented by performing *post-mortem* x-ray computed microtomography scans. However, such *operando* characterization does not allow 3D information to be collected at key stages of the layer-by-layer process. One could also argue that looking at single tracks is not necessarily representative of what is going on while fabricating a 3D object made of adjacent molten tracks and stacked layers.[18] In addition, scanning strategies are known to play a role in defect formation and spatial distribution. Beam path and speed often need to be adjusted to prevent defect formation. For example, heat concentration might occur when applying a snake-like hatching strategy if delays or adapted beam speed profiles are not optimized. Molten track stability may also strongly be altered by local variations of the powder bed, the most striking example being denudated zones.[1,19] Finally, a few layers are often required for the steady-state to be established. This non-exhaustive list of examples shows that a 3D characterization of bulk parts fabricated by L-PBF instead of a single molten track would certainly benefit the AM community.

We have recently designed and introduced a miniature L-PBF replicator to extend the *in situ* characterization of powder bed fusion AM-processes to 3D[20] to fill in this technology gap. Few illustrative examples based on single tracks were used to demonstrate the technical feasibility of the approach.[20] This new characterization approach not only fills a technical gap but also allows key information that is not yet available to be collected in conditions that are thought to be closer to the ones of more commercial machines.

The most interesting feature that can be captured using such a characterization approach is certainly the evolution of the defect population and linking it to the scanning strategy. Indeed, defect population can be monitored in 3D throughout a build and reveal mechanisms such as pore nucleation and growth or eventually healing while processing new layers. In the case of complex structures, such as lattice structures, this is even more crucial since the local melting conditions are uneven: small diameters (<0.5 mm), overhang surfaces, and the presence of nodes can induce significant heterogeneities under local thermal conditions. One can also obtain key information regarding the evolution of the dimensions of the fabricated parts or the roughness of the different surfaces of a sample. The material volume added at each layer can also be estimated. The 3D characterization of the powder bed can also be done to provide data regarding the topology and the local arrangement of the powder bed and, possibly, regarding the size and volume distribution of denudated zones.

In this work, we provide further experimental validation demonstrating the reliability of the proposed characterization approach. 3D bulk samples with a base of 4 × 4 mm and a height of a few tens of layers were first fabricated using our replicator and characterized post-mortem using laboratory x-ray computed tomography. Then, similar 3D samples were fabricated and characterized *in situ* with the replicator installed on the BM05 beamline of the European Synchrotron Radiation Facilities (ESRF). Ultimately, we also give a first example showing that the fabrication of more complex 3D parts such as a lattice unit cell can also be considered.

II. L-PBF REPLICATOR DESIGN

A. L-PBF replicator

The L-PBF replicator consists of two different devices: an energy source (laser and scan head) and a custom-designed build chamber allowing x-ray 3D images to be collected at key stages of the process. It means that such a replicator is highly versatile as the energy source could be changed relatively easily (pulsed laser, a laser with different wavelengths: green, blue laser).

A mono-mode fiber laser source (wavelength equal to 1080 nm) from SPI (QUBE 500 W) delivering a maximum power of 500 W was used in this work. A ScanLab HSC II 14 scanning head was employed. A motorized galvanometric mirror allows the beam motion and position to be controlled. An f-theta lens from Linos is used to focus the laser beam at a distance of roughly 500 mm from the scanning head. The scanning head is mounted on an aluminum frame fixed on a motorized elevator to accurately adjust the vertical position of the scanning head. This is crucial because the laser beam must be focused at a specific position as will be explained later. Adjustment of the focal distance was performed by visual inspection of static laser shots on an anodized aluminum plate at different heights.

An overview of the custom-designed L-PBF replicator is shown in Fig. 1. The upper part of the replicator is the build chamber made of a polycarbonate tube transparent to x rays. The top cover is made of stainless steel, and the porthole is equipped with a treated glass absorbing less than 0.5% of the laser power. The build chamber is sealed and is connected with valves to a vacuum pump and a gas inlet allowing one to use of a controlled atmosphere. Two O-ring seals are employed to seal the chamber and hold the polycarbonate

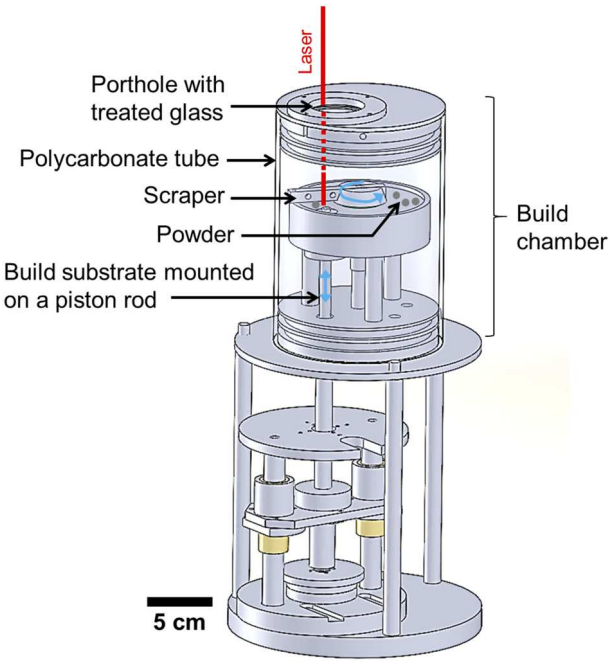

FIG. 1. 3D CAD-view of our custom-designed L-PBF replicator.

tube. Before running an experiment, oxygen was first purged from the sealed chamber using three repeated cycles of vacuum pumping using an LS63P/T primary vacuum pump from Edwards (down to 0.1 mbar) and argon flow. During the experiments, Ar was continuously flowed in the build chamber to mimic the situation of more commercial L-PBF machines. The gas inlet was positioned so that to be as close as possible to the building substrate in its lasing position. An oxygen sensor, a ZRA II MP from Arelco, was implemented to measure the oxygen content during the tests. The sensor operates with a small vacuum pump to sample the atmosphere chamber. All experiments were conducted at contents below 100 ppm of oxygen.

The building substrate is a disk, 8 mm in diameter in this case, mounted on a piston that moves up and down. The position of the build plate is controlled with a ±5 μm accuracy and a maximal displacement rate of 0.5 mm/s. Two different configurations are of interest depending on the position of the piston and are schematically described in Fig. 2. The first configuration corresponds to the coating position when the piston is down. For powder deposition, a scraper is rotated around the central rotation axis of the system to coat the building substrate with a new powder layer. Coating occurs when the piston is down (coating position) as shown in Fig. 2(a).

Once powder coating is done, the piston moves up at a displacement rate of 0.5 mm/s in a shadow-free position allowing x-ray tomography scans to be acquired [Fig. 2(b)] without missing angles because the replicator is positioned on a rotating stage dedicated to x-ray 3D imaging. Note that we did not notice any evolution of the powder bed in the region of interest during the elevation and retraction of the build plate for builds consisting of 30 layers, except on the periphery of the build plate. Typically, a region of about 0.5 mm was affected along the periphery of the build plate.

The focal distance was adjusted so that the piston was in its shadow-free position and was kept the same throughout the build, the piston being in charge of positioning the sample height for melting, while the laser is able to scan in X and Y. The laser scan head was controlled using a *sky-writing* option allowing the laser to be activated only when the mirrors move at a constant speed, thus delivering a steady scan rate on the whole length of the laser tracks. The laser beam goes through a porthole equipped with a treated glass and hits the powder bed. For each layer processed, two scans are acquired: the first one after powder deposition and the second one after selective laser melting. This gives a unique opportunity to collect 3D information regarding the topology of the powder bed, the evolution of the defect population while adding layers, and to quantify the material added to the part at each layer. Control of both build plate motion and scraper rotation is ensured by dedicated software.

A high-speed camera was also implemented to monitor the laser scan speed and to evaluate qualitatively the spattering tendency depending on the applied processing parameters. However, the design of the replicator requires the use of a mirror so that the camera can monitor the region of interest while not interfering with the laser. We recorded 3200 images per second with an aperture time of 10 μs and a resolution of 1280 × 800 pixels^2. An example of a video recorded during an experiment conducted at the ESRF (BM05 beamline) using the high-speed camera is shown in Fig. 3 (multimedia view 3).

B. Material

As the objective of this study was to benchmark our L-PBF replicator designed for 3D x-ray imaging under synchrotron radiation, we used the most widely used material in AM, i.e., Ti6Al4V. The powder batch employed in this work was gas atomized and, therefore, had a spherical geometry with a size distribution determined by laser granulometry between 15 (D10) and 45 μm (D90), as typically encountered in L-PBF.

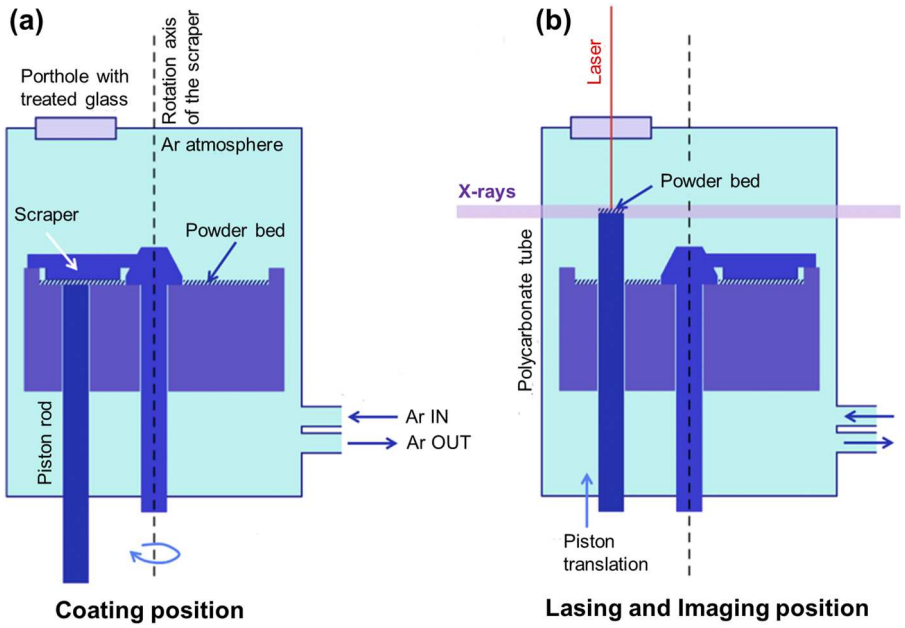

FIG. 2. Schematics showing the two configurations of the system: (a) coating position (piston down) and (b) lasing and imaging position (piston up).

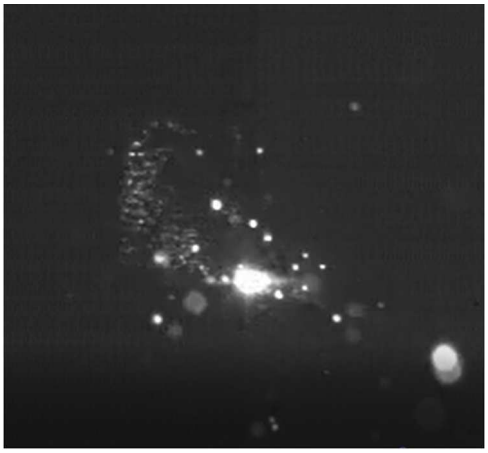

FIG. 3. Example of a snapshot of a video (multimedia view 3) acquired using a high-speed camera during an experiment conducted at the ESRF. Multimedia view: https://doi.org/10.1063/5.0090623.1

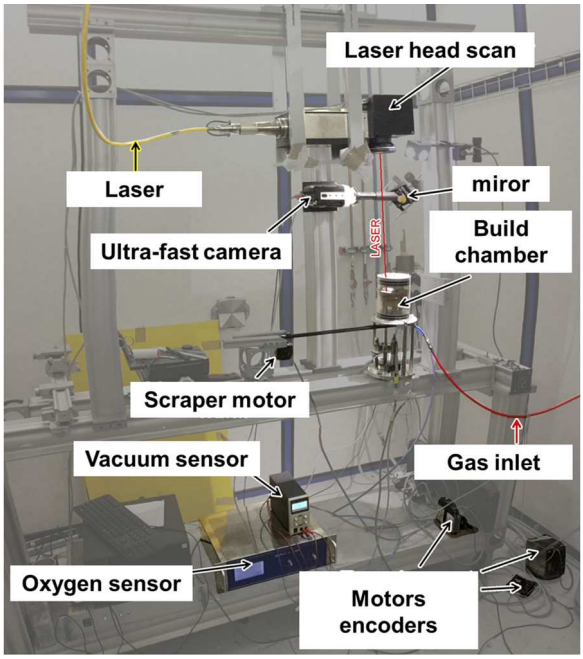

FIG. 4. Experimental setup used to build samples using the L-PBF replicator before beamline implementation.

III. PRELIMINARY VALIDATION USING POST-MORTEM X-RAY COMPUTED TOMOGRAPHY SCANS

A. Processing and imaging conditions

The L-PBF replicator was first validated before beamline integration by fabricating cube samples with a 4 mm edge. The experimental setup is described in Fig. 4. Note that the same experimental setup will be used on the ESRF BM05 beamline. Laser power was kept constant at 150 W with a spot size of 70 μm while the scanning speed was varied between 1000 and 2000 mm/s. A hatching lasing strategy consisting of moving the beam in a snake-like way with a hatch spacing of 0.11 mm was employed (no specific scanning strategy was used to melt the contours). The hatching direction was rotated by 90 °C between each layer. Three samples were built using a layer thickness of 50 μm and one with a layer thickness of 30 μm. The processing conditions associated with each cube are given in Table I. Such conditions were chosen based on the literature[21,22] with the objective to produce samples with different lack-of-fusion defect densities. Sample fabrication was considered successful when at least 20 layers were processed. Note that with the parameters applied here (volume energy density $VED = E_V\ P/(v.S)$ with S = spot surface between 19 and 38 J/mm^3), we expected to be in a fusion regime mostly governed by conduction heating, i.e., without extended vaporization.

The fabricated cube samples were then characterized by x-ray microtomography. Scans were acquired with an EasyTom XL tomograph (RX-solution). 1056 projections (exposure time of 1.5 s) over 360° were acquired for each sample using an x-ray incident beam (150 kV, 60 μA) filtered by 0.5 mm of copper and a geometric magnification of 8.5, which results in a voxel size of 15 μm. 3D volumes were reconstructed with the Xact software using a standard filtered back-projection algorithm. The fabricated samples exhibiting a relative density >95% were then further characterized using optical microscopy and microhardness measurements using a load of 1 kgf. Optical cross sections were prepared by grinding down to P4000 and polishing for 20 min with a solution consisting of 80% colloidal silica and 20% H_2O_2. The microstructure was revealed by chemical etching using Kroll's reagent.

B. Validation via post-mortem analyses

Pictures taken once the sample fabrication was completed are shown in Figs. 5(a)–5(c) for different processing conditions. As no supports were used, the samples were welded to the cylindrical build substrate attached to the moving piston. The sample relative density was estimated based on the 3D reconstructed volume from XCT scans (voxel size 15 μm). As expected, the build quality improves while increasing the energy input (E_l) from 75 J/m to 150 J/m with relative density increasing from 86% to 99.8%. To estimate the error made while analyzing the porosity by thresholding the grayscale image, we applied two additional thresholds. The first threshold was made so as to slightly overestimate the pore diameter while the second one leads to a slight underestimation of the pore diameter. It was concluded that the error made on the pore diameter was below 3%; this is not surprising given the very good contrast between the material and the pore in the 3D images. This was considered negligible. The build quality can be further appreciated based on the 2D longitudinal cross sections extracted from the middle of the 3D reconstructed volume of the fabricated samples shown in Figs. 5(a)–5(g). Those results can be considered as proof that 3D bulk samples can be successfully built using our custom-designed L-PBF replicator. Note that the 2D cross sections extracted from the middle of the fabricated samples are not necessarily representative of the overall porosity measured based on the full reconstructed volume. This is a well-known artifact when looking at 3D features

TABLE I. Summary of the processing conditions of various cube samples prior to beamline integration.

	Power, P (W)	Scan speed, v (mm/s)	Layer thickness, e (mm)	Hatch spacing, h (mm)	Linear energy, E_l (J/m)	VED, E_V (J/mm^3)
Sample 1		2000			75	20
Sample 2	150	1500	0.05	0.11	100	26
Sample 3		1000			150	39
Sample 4		1500	0.03		100	26

(pores) using 2D images, the latter being particularly true when such features are heterogeneously distributed as shown later in this article; see, e.g., Fig. 10.

As one of the most interesting features that can be captured with the characterization approach proposed in this work is the evolution of the defect population while processing new layers, we deliberately produced samples with lack-of-fusion defects. Samples 1 and 2 deliberately produced with a low energy input to induce lack-of-fusion defects were analyzed to reveal the distribution of the defects within the samples based on XCT scans. Figure 6 shows axial cumulative projection views of samples 1 and 2, respectively. Such analysis allows the distribution of defects to be revealed by computing the local relative density along a given axis. Lacks-of-fusion are known to form preferentially in overlapping areas between adjacent molten tracks. Given the scanning strategy employed to build those samples, lacks-of-fusion are expected to be distributed periodically in the materials with a characteristic length corresponding to the hatch spacing as typically reported in Refs. 23–25. The latter idea is supported by the analysis shown in Fig. 6 where the local density exhibits a lower value in regions separated by roughly 100 μm and the hatch spacing is 110 μm.

To go a step further in the benchmarking of our replicator, we have compared the build quality of the samples fabricated using our device with the processing window of Ti6Al4V found in the literature. Optical micrographs of samples (10 × 10 × 5 mm^3) fabricated with an EOS M270 L-PBF machine using different powers and scan speeds (extracted from[21]) are shown in Fig. 7 where we have also included a 2D slice extracted from the 3D reconstructed volume of the samples built using our replicator [Figs. 7(a)–7(d)]. Based on Ref. 21, the optimal linear energy density should be between 130 and 200 J/m to achieve a high density. Below 130 J/m, lack-of-fusion defects are expected, and above 200 J/m, keyhole pores

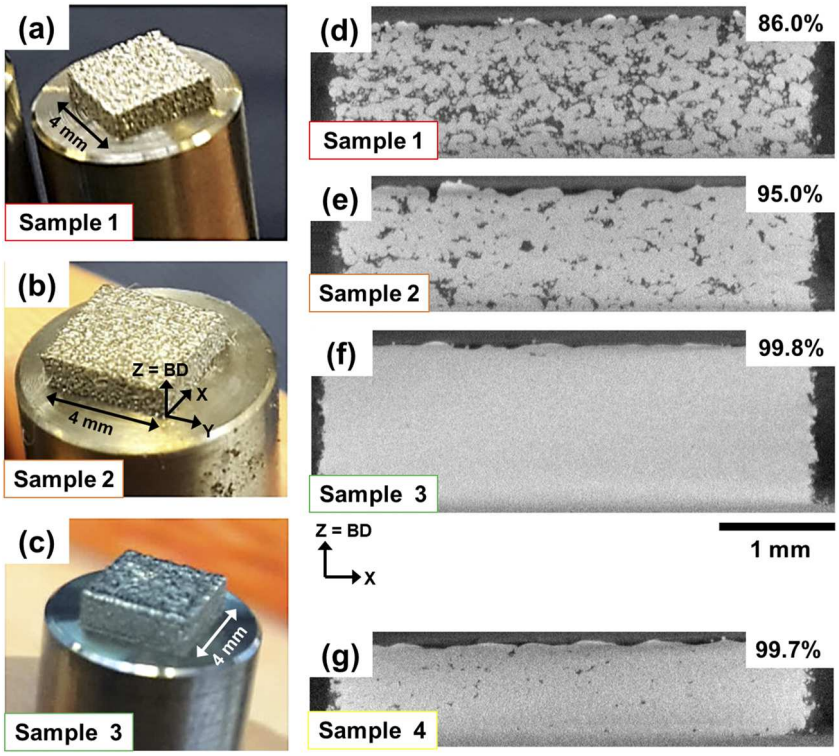

FIG. 5. Pictures of some fabricated 3D cubes on the build substrate mounted on a piston: (a) sample 1 (P = 150 W, v = 2000 mm/s, and e = 0.05 mm); (b) sample 2 (P = 150 W, v = 1500 mm/s, and e = 0.05 mm); and (c) sample 3 (P = 150 W, v = 1000 mm/s, and e = 0.05 mm). 2D longitudinal cross sections (X, Z) extracted from the center of the reconstructed volume to give an idea of the defect density: (d) sample 1, (e) sample 2, (f) sample 3, and (g) sample 4 (P = 150 W, v = 1000 mm/s, and e = 0.03 mm). The relative density estimated based on the reconstructed volume is also given.

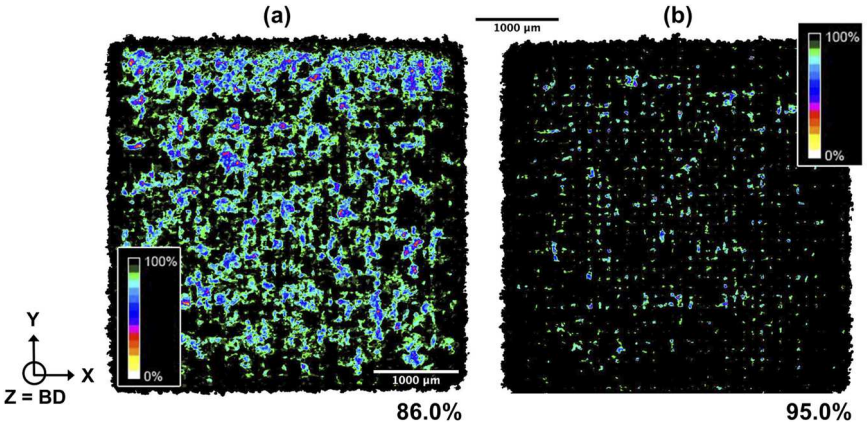

FIG. 6. Axial cumulative projected view of all the slices along with the height (build direction) of the sample: (a) sample 1 (75 J/m) and (b) sample 2 (100 J/m). Color code shows the local relative density: white means that a pore goes through the entire sample height while black means that the sample is locally fully dense.

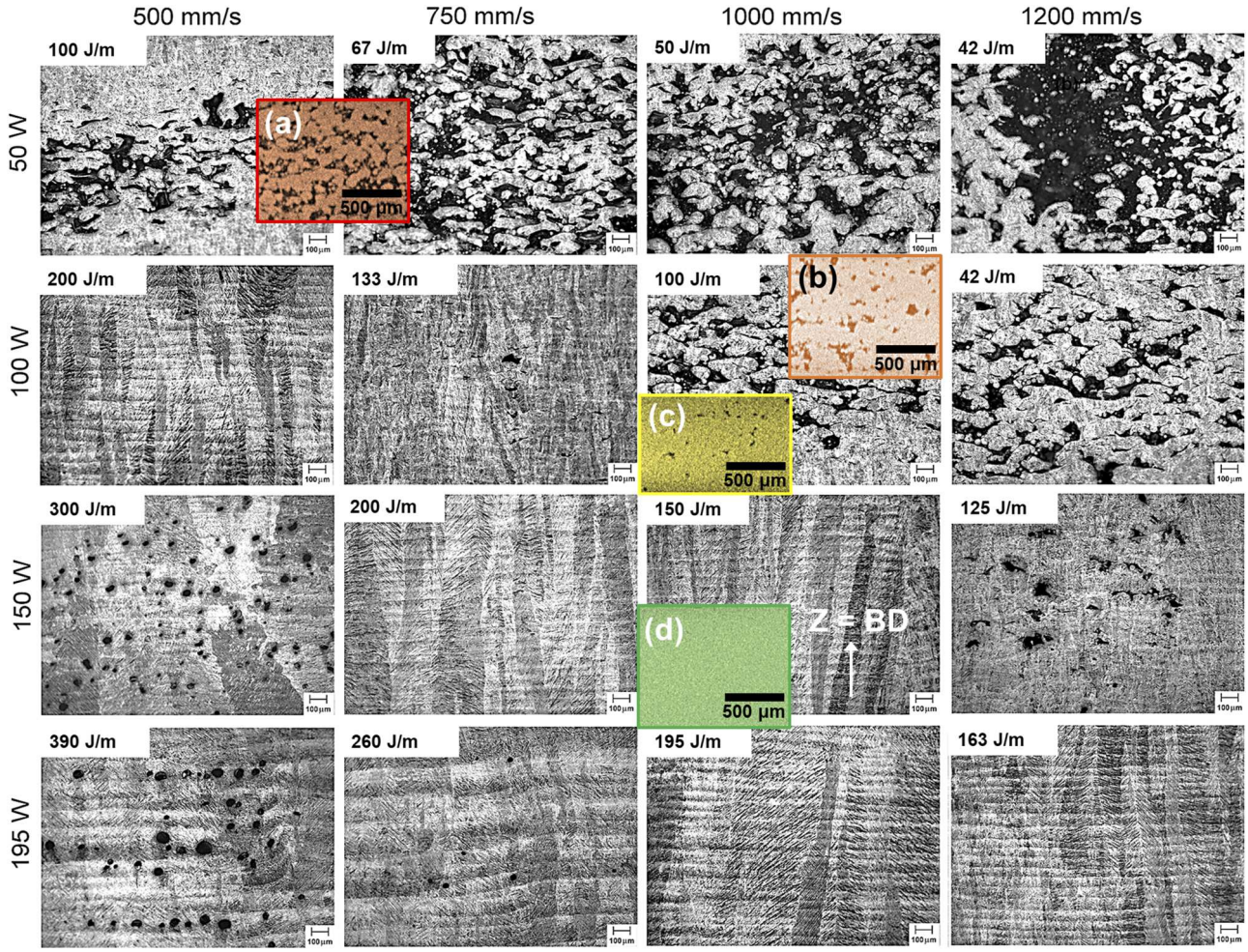

FIG. 7. (a) Position of the fabricated cubes in the processing window of Ti6Al4V fabricated by L-PBF. Adapted with permission from Dilip *et al.*, Prog. Addit Manuf. **2**,157–167 (2017). Copyright 2017 Springer Nature:[21] (a) sample 1 (75 J/m, 86.0%); (b) sample 2 (100 J/m, 95.0%); (c) sample 4 (99.7%, 100 J/m); and (d) sample 3 (150 J/m, 99.8%). Images are random 2D cross sections (X, Z) extracted from the center of the sample. The building direction lies vertically on the page for all images.

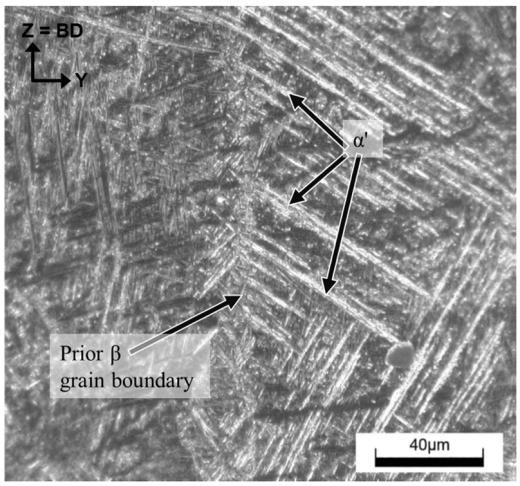

FIG. 8. Optical micrograph taken in sample 3 after chemical etching (Kroll reagent) revealing the presence of fully α'-martensitic microstructure under the as-fabricated conditions.

are observed. Similar linear energy inputs lead to very close build quality demonstrating that the processing conditions in our custom-designed replicator are close to the ones applied in commercial machines.

Samples with a relative density >99.5% were also examined by optical microscopy and hardness measurements were also carried out to compare with results reported in the literature for dense Ti6Al64V samples fabricated with commercial machines. The as-fabricated microstructure shows the presence of α'-martensite within prior β columnar grains that grew along the building direction as exemplified by the optical micrograph of sample 3 shown in Fig. 8 with its characteristic needle-like morphology as typically found in the literature.[26,27] Prior β grains with a columnar morphology can also be observed The average hardness (computed over 30 measurements) of samples 2, 3, and 4 was found to vary between 350 and 380 HV in agreement with various studies reporting hardness values between 350 and 400 HV.[22,26] For instance, the hardness of the sample with the highest relative density (sample 3) was found to be 360 ± 10 HV. Those results contribute to benchmarking our L-PBF replicator.

IV. EXPERIMENTAL VALIDATION ON A SYNCHROTRON IMAGING BEAMLINE AT ESRF

A. Beamline implementation, imaging conditions, and image analysis procedures

The L-PBF replicator consisting of the laser (source and scanning head) and build chamber was integrated into the beamline BM05 of the ESRF, as shown in Fig. 9. The laser scanning head is held by a camera manipulator as shown in Fig. 9 and mounted on a motorized stage allowing the scanning head to be accurately positioned so that the laser can go through the dedicated porthole and hit the region of interest. The focal distance was adjusted to give the smallest spot size when the building substrate is in its lasing position, as shown in Fig. 2(b). The build chamber was placed on the

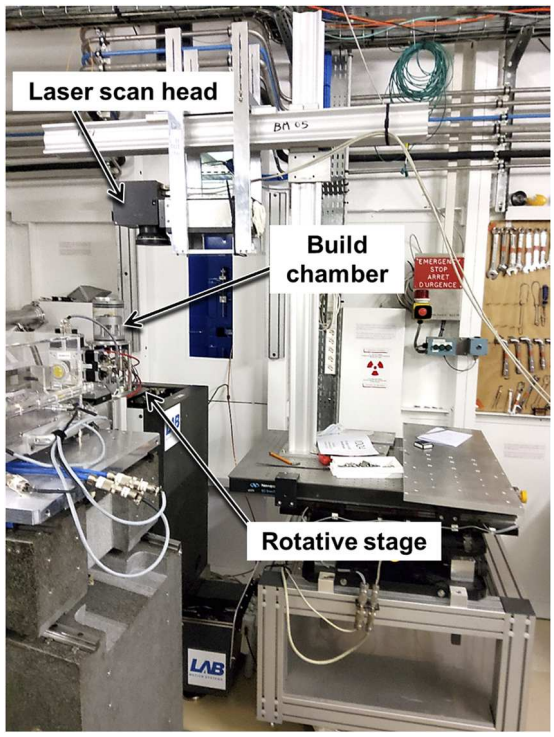

FIG. 9. Picture showing the integration of the L-PBF replicator: laser and build chamber at beamline BM05 of the ESRF.

Leuven medium resolution rotating stage. Cables ensuring connection were attached in such a way to allow 180°-rotation of the build chamber.

Safety issues are overcome by interlocking the laser source to the experimental hutch door of the beamline BM05 of the ESRF. Thus, no laser emission is possible when the hutch door is open.

An indirect x-ray image detector, the so-called "zoom optic" (Continuous magnification from 1X to 5X, ESRF Detector Unit development, designed by Christophe Jarnias and Paul Tafforeau) was used: consisting of a scintillator lens-coupled (Canon super macro MPE 65 mm) to an sCMOS camera (type: pco.edge 4.2 CLH, PCO AG, Germany). Image acquisitions were made using the absorption contrast using a magnification of 1.625X. Such a magnification results in a voxel size of 4.00 μm. A 250 μm thick LuAg was used as a scintillator. A ring current of 200 mA was used throughout the experiments. A pink beam was employed using the two poles wiggler (2× 0.856 T, 18 mm fixed gap) filtered with 2.59 mm of copper and 8 mm of SiO_2 bars. This results in an average detected energy of 88.6 keV. The distance between the sample and the detector was about 1400 mm. Exposure time was set to 12 ms. 2000 projections were acquired per scan resulting in a scan time of 25 s including reference images. A region of interest (ROI) of 2048 × 640 pixels^2, which results in a field of view of 8.2 × 2.56 mm^2, was used.

The ESRF fasttomo3 pre-processing and PyHST2 routines were applied for the 3D reconstruction of the data[28] using classical filtered back-projection algorithms. An in-house ESRF-Matlab routine was used for post-reconstruction ring removal.[29] Reconstructed volumes

were cropped to select the ROI and converted to 8-bits while using a fixed grayscale range per sample. Fiji[30] and in-house plug-ins[31] were used for image analysis. A virtual powder removal procedure, see more details in Ref. 20, has been developed and makes it possible to achieve 3D rendering of the fabricated objects throughout the layer-by-layer building sequence. Briefly, the virtual view is a 3D view of the built object as it would be observed if the powder bed was removed. Virtual powder removal was performed using image processing based on morphological operators consisting of a combination of a basic cutoff threshold value determined by iterative intermeans, 3D hole filling, 3D opening (erosion and dilation) using an exact Euclidean distance, 3D flood filling, and classical Boolean operations. This image analysis routine removes powder particles whose contact surface with the melted objects shows a radius smaller than 24 μm (six voxels).

B. Validation at ESRF

Two 3D objects with a base section of 4×4 mm^2 with a height of about 20–30 layers were built on the beamline BM05 of the ESRF to validate our experimental setup for a 3D *in situ* characterization of L-PBF. A hatching lasing strategy consisting of moving the beam in a snake-like way with a hatch spacing of 0.11 mm was employed with a 90°-rotation of the hatching direction between each layer (no specific scanning strategy for contouring). During those experiments, the typical time to achieve a whole cycle as described in Sec. II A, powder deposition (≈5 s), piston up (≈5 s), XCT-scan (25 s in this case), printing (≈1 s), XCT-scan (25 s in this case), and piston down (≈5 s), was estimated to be of the order of 1 min. This time is of the same order of magnitude as the time required to build a layer in a commercial machine considering that only one small object with a size close to the one fabricated in this work would be printed. If needed, the time required for a whole cycle could be reduced down to about 20 s. Here, the energy input was deliberately chosen to build a sample in conduction mode (sample B, energy input close to that of sample 3) and the other in a keyhole regime (sample A) because such a melting regime was not explored during our lab validation using post-mortem XCT-scans; see details in Table II.

Figure 10 (multimedia view 10) shows 3D renderings of virtual views of the fabrication of sample A after processing of different layers. Those virtual views can be used to monitor a build while adding layers. Interestingly, in the example shown in Fig. 10 (multimedia view 10), our approach reveals the link between the scanning strategy and the spatial distribution of pores (displayed in red) within the sample. Pores seem to be preferentially located along the edge of the melted area where the hatching ends. For example, at layer 1 [Fig. 10(a)], the hatching direction is from right to left (scanning direction parallel to X) and pores are mostly located along the left edge of the melted area, the center of the melted area being almost defect-free. At layer 2, the hatching direction is rotated by 90° and is now from top to bottom (scanning direction parallel to Y). Pores generated while processing layer 2 are now preferentially located along the bottom edge of the melted area; see Fig. 10(b). At layer 3, the hatching direction is once again rotated by 90° (scanning direction parallel to X) and is now from left to right. Pores generated while processing layer 3 are mostly located along the right edge of the scanned area [Fig. 10(c)]. Finally, at layer 4, the hatching direction is rotated by 90° (scanning direction parallel to Y) and pores are found along the top edge of the scanned area; see Fig. 10(d). As the hatching direction is rotated by 90° at each layer, after four layers, the four edges are decorated with pores and this mechanism is repeated while processing new layers. We recall here that the processing parameters used to produce sample A were chosen to generate keyhole pores. Those defects located along the periphery of the scanned area are keyhole pores[16,32–34] with their typical spherical morphology, as illustrated in Figs. 11(a) and 11(b). A quick analysis of the defect population found in sample A and consisting in plotting the pore sphericity as a function of their equivalent radius [Fig. 11(c)] confirms the rather spherical morphology of the pores and supports the idea that those defects are indeed keyhole pores. At a first sight, the spatial distribution of those keyhole pores can be surprising because one could expect the presence of keyhole pores in the whole scanned area. Here, keyhole pores are exclusively found along the last molten track. This is because keyhole pores generated while scanning the $(n-1)$th track are thought to be suppressed while melting the nth track due to large overlapping areas between adjacent molten tracks. Thus, keyholes formed during the last molten track cannot be suppressed. Figure 10 (multimedia view 10) shows a first illustrative example that shows how one can take advantage of the layer-by-layer 3D characterization of L-PBF made possible by the use of our miniature laser powder bed fusion system. A video file of the fabrication of this sample is also provided in Fig. 10 (multimedia view 10).

Figure 12 (multimedia view 12) shows 3D renderings of virtual views of the fabrication of sample B after processing of different layers. Here, the processing conditions were selected to be close to the processing window identified in Fig. 7. Thus, nearly fully dense samples are expected. The 3D characterization shows that indeed the sample fabricated has a relative density higher than 99.9% with the spatial resolution employed here (voxel size 4 μm, features smaller than 10 μm cannot be captured properly). A video file of the fabrication of this sample is also provided in Fig. 10 (multimedia view 10). In such a case, monitoring the defective population shows a limited interest but other interesting characteristics can be highlighted and are better illustrated in Fig. 13. Figure 13 reveals the evolution of a specific region of interest located near the edges of sample A based

TABLE II. Summary of the processing parameters used to build samples at the BM05 beamline of the ESRF.

	Power, P (W)	Scan speed, v (mm/s)	Layer thickness, e (mm)	Hatch spacing, h (mm)	Linear energy (J/m)	VED, E_V (J/mm^3)
Sample A	150	250	0.05	0.11	600	156
Sample B	150	750	0.03	0.11	200	52

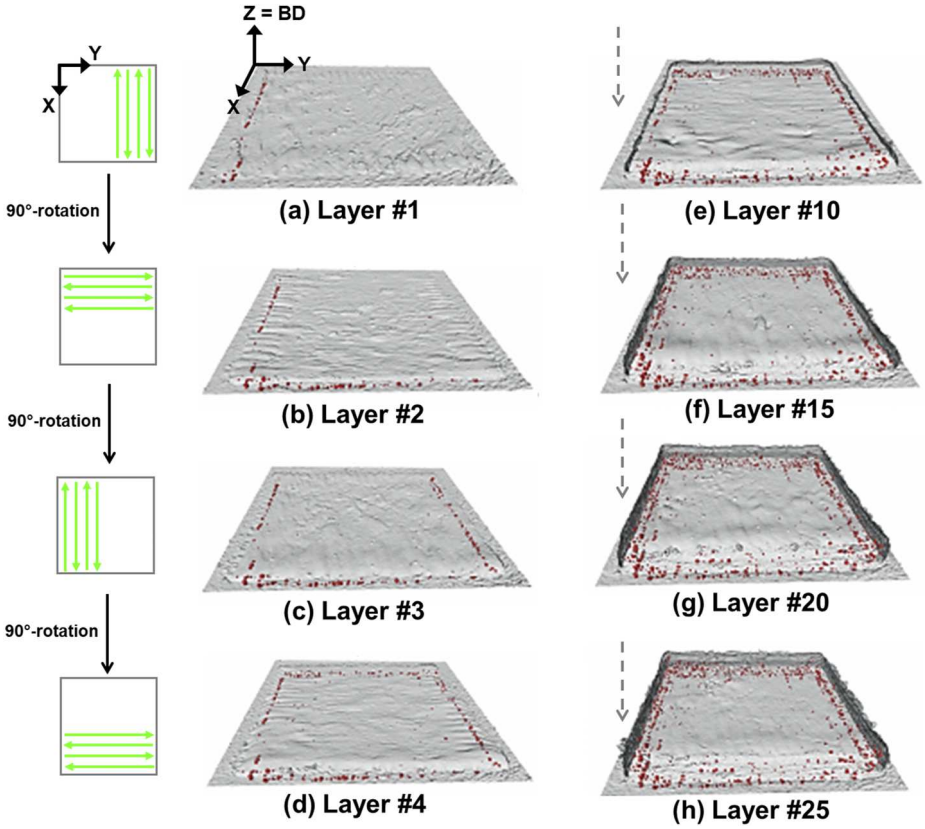

FIG. 10. (a)–(h) 3D rendering of sample A under fabrication at different layers. Here, P = 150 W and v = 250 mm/s resulting in a keyhole regime (multimedia view 10). The scanning strategy is indicated using schematics so that links between the spatial distribution of defects within the sample and the scanning strategy can be established. Pores are displayed in red. The edge of the scanned area is 4 mm. Multimedia view: https://doi.org/10.1063/5.0090623.2

on 2D cross sections taken from 4 consecutive layers and extracted at a given height. In Fig. 13(a), at the edges of the scanned area where molten tracks start or end, traces of isolated molten tracks can be seen and show that the contours of the melted area are not well defined. At the next layer, see Fig. 13(b), the hatching direction is rotated by 90° and this is shown to correct the contour defect highlighted in Fig. 13(a). The next layer is processed by rotating again the hatching direction by 90° and the contour defect is highlighted again [Fig. 13(c)] but will be corrected while processing the next layer; see Fig. 13(d). Such an example shows that L-PBF is a process that generates some defects that can lead to numerous defects but a large proportion of these defects can be corrected while processing the next layers. This idea was also supported in a previous paper where we showed that some pores generated while processing a given layer

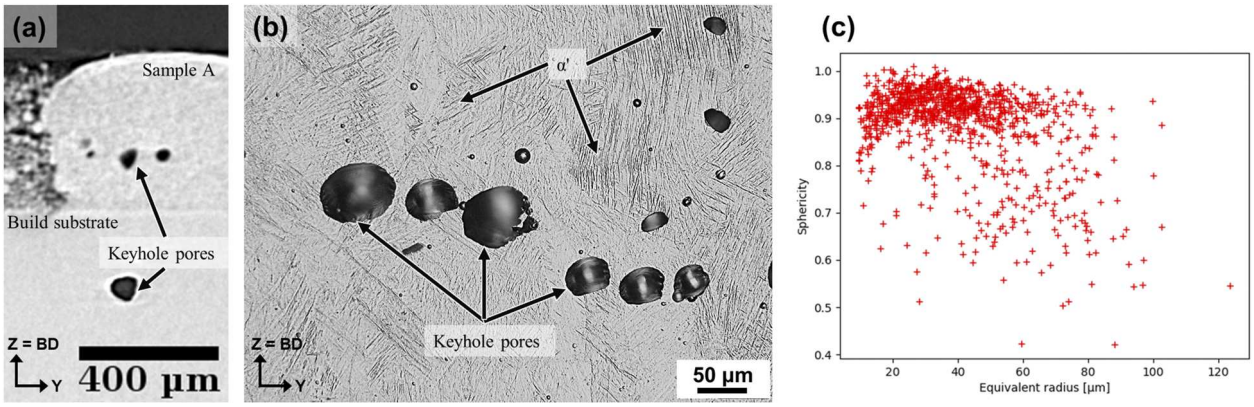

FIG. 11. (a) 2D cross section extracted from the edge of sample A and showing the presence of keyhole pores. (b) Optical micrograph revealing the martensitic microstructure and the presence of keyhole pores. (c) Analysis of the pore population in sample A: sphericity vs equivalent radius.

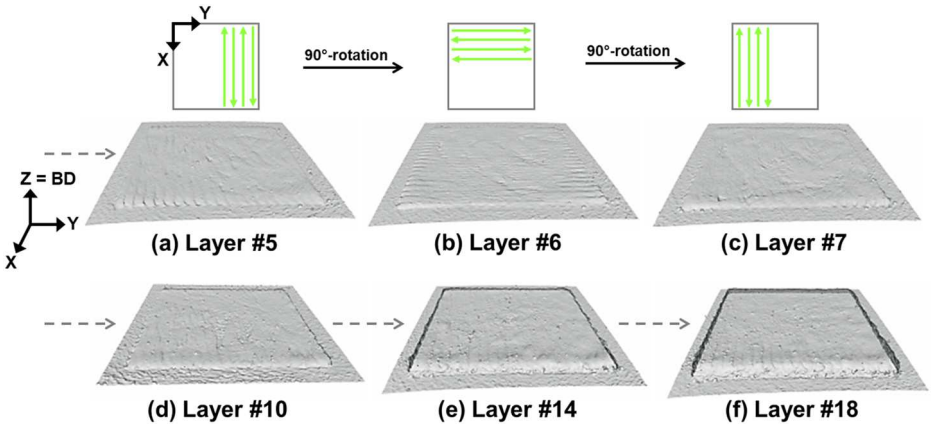

FIG. 12. (a)–(f) 3D rendering of sample B under fabrication at different layers. Here, P = 150 W and v = 750 mm/s resulting in a conduction regime (multimedia view 12). The scanning strategy is indicated using schematics. Pores are displayed in red. The edge of the scanned area is 4 mm. Multimedia view: https://doi.org/10.1063/5.0090623.3

can be healed while processing the next few layers.[20] Interestingly, it means that a large proportion of defects generated during L-PBF can be self-healed due to the layer-by-layer nature of this process.

As a last experimental validation of our miniature L-PBF system making possible a layer-by-layer 3D characterization, we started building more complex geometries. Figures 14(a)–14(h) shows a promising example where the first layers of lattice structure BCC-Z unit cell consisting of 1 mm diameter struts were processed. After ten layers, even though the employed processing parameters have not been optimized for lattice structures, one can clearly distinguish vertical and 45°-oriented struts. A full video of the layer-by-layer fabrication of this unit cell based on 3D reconstructions is given in Fig. 14 (multimedia view 14) along with a video acquired using the high speed camera; see Fig. 15 (multimedia view 15). This video is also useful to illustrate the spiral scanning strategy employed here. Note that some pores, displayed in red, can be seen in the fabricated struts. The latter are thought to be keyhole pores because of

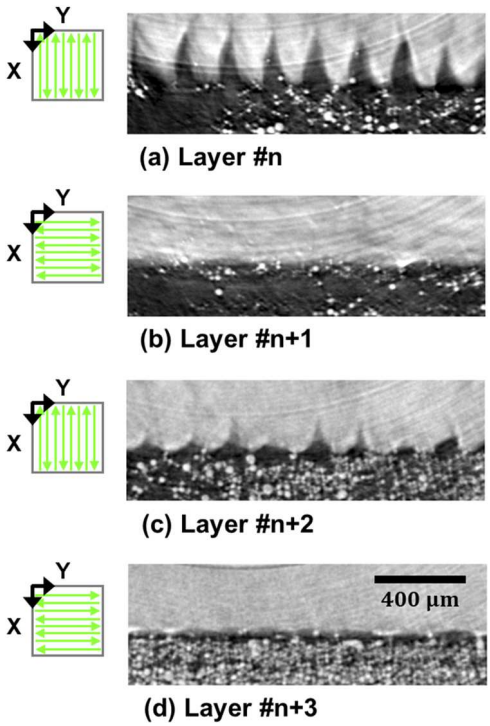

FIG. 13. 2D cross sections (X, Y) extracted from the reconstructed volume of sample B at a given height (Z position fixed). Four consecutive layers are shown: (a) Layer #n, (b) Layer #n + 1, (c) Layer #n + 2, and (d) Layer #n + 3. For each layer, the scanning strategy is schematically represented.

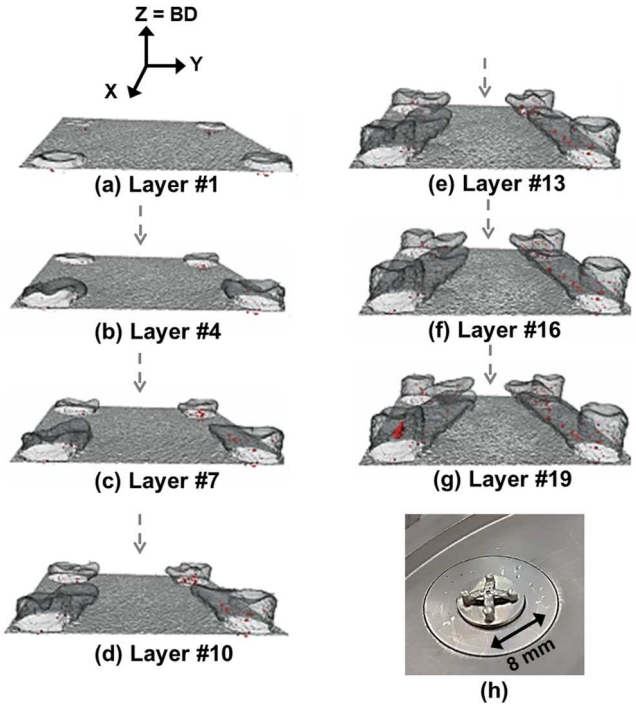

FIG. 14. (a)–(g) 3D rendering of the build history of the first layers of fabrication of a lattice structure unit cell (multimedia view 14). (h) Picture of the first layers of a lattice unit cell built using our miniature laser powder bed fusion. Multimedia view: https://doi.org/10.1063/5.0090623.4

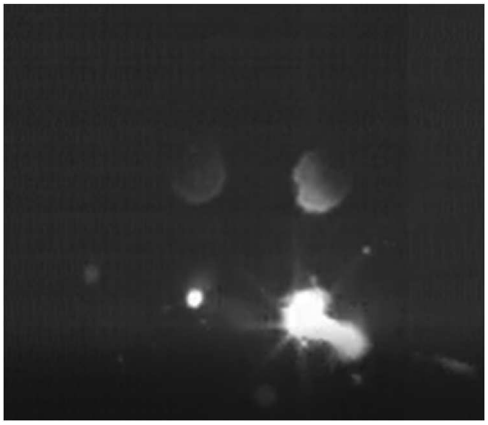

FIG. 15. Example of a snapshot of a video (multimedia view 15) acquired using a high-speed camera while building a lattice unit cell at the ESRF. Multimedia view: https://doi.org/10.1063/5.0090623.5

the energy input used to build the struts (P = 150 W, v = 500 mm/s, and E_V = 78 J/mm^3). The rounded morphology of the pores is typical of keyhole defects.[16,32]

V. CONCLUSION

We have described a miniature L-PBF replicator compatible with the constraints imposed by 3D x-ray imaging using synchrotron sources. This instrument allows extending the *in situ* characterization of laser powder bed fusion to 3D. The building atmosphere can be controlled, and the building substrate is mounted on a piston that can move up (lasing and imaging in a shadow-free position) and down (coating position). This replicator was validated using *post-mortem* x-ray computed tomography scans to demonstrate that samples can be produced in conditions representative of commercial L-PBF machines. This device was then integrated into the BM05 beamline of the ESRF so that 3D images can be acquired layer by layer. We show, based on a few illustrative examples, that such an approach allows us to track defect population throughout a build and eventually link it to the scanning strategy employed. A better description of the powder bed: local density, 3D arrangement, and packing, size of the denudated zones (not illustrated in this paper) can be achieved and allows establishing some links with defects formation. Those aspects are often poorly addressed in the literature due to the lack of the third dimension and will be investigated in more detail shortly using our miniature laser powder bed fusion system for synchrotron 3D imaging. This replicator is thought to open new paths to improve our current understanding of the L-PBF process and can be seen as a complementary characterization approach in comparison to replicators enabling us to shed light on various dynamic mechanisms involved in the molten bead formation.

ACKNOWLEDGMENTS

This work was performed within the framework of the Centre of Excellence of Multifunctional Architectured Materials "CEMAM" n°AN-10-LABX-44-01 funded by the "Investments for the Future Program." The European Synchrotron Radiation Facility (ESRF) was gratefully acknowledged for offering beamtime associated with Grant No. MA4066.

AUTHOR DECLARATIONS

Conflict of Interest

The authors have no conflicts to disclose.

Author Contributions

Pierre Lhuissier: Conceptualization (lead); Data curation (lead); Formal analysis (lead); Investigation (lead); Methodology (lead); Resources (lead); Software (lead); Supervision (equal); Validation (lead); Visualization (lead); Writing – review & editing (equal). **Louis Hébrard:** Data curation (equal); Formal analysis (equal); Investigation (equal); Methodology (supporting); Visualization (equal). **Xavier Bataillon:** Methodology (supporting). **Pierre Lapouge:** Investigation (supporting); Methodology (equal); Validation (equal); Writing – review & editing (supporting). **Frédéric Coste:** Methodology (supporting). **Patrice Peyre:** Investigation (equal); Methodology (equal); Supervision (lead); Validation (equal); Writing – review & editing (supporting). **Elodie Boller:** Investigation (supporting); Methodology (supporting); Software (supporting). **Jean-Jacques Blandin:** Funding acquisition (lead); Supervision (supporting); Writing – review & editing (supporting). **Luc Salvo:** Investigation (supporting); Methodology (supporting); Writing – review & editing (supporting). **Guilhem Martin:** Formal analysis (equal); Investigation (supporting); Methodology (supporting); Supervision (lead); Validation (equal); Writing – original draft (lead); Writing – review & editing (lead).

DATA AVAILABILITY

The data that support the findings of this study are available from the corresponding authors upon reasonable request.

REFERENCES

[1]M. J. Matthews, G. Guss, S. A. Khairallah, A. M. Rubenchik, P. J. Depond, and W. E. King, "Denudation of metal powder layers in laser powder bed fusion processes," Acta Mater. **114**, 33–42 (2016).

[2]V. Gunenthiram, P. Peyre, M. Schneider, M. Dal, F. Coste, I. Koutiri, and R. Fabbro, "Experimental analysis of spatter generation and melt-pool behavior during the powder bed laser beam melting process," J. Mater. Process. Technol. **251**, 376–386 (2018).

[3]S. Ly, A. M. Rubenchik, S. A. Khairallah, G. Guss, and M. J. Matthews, "Metal vapor micro-jet controls material redistribution in laser powder bed fusion additive manufacturing," Sci. Rep. **7**, 4085 (2017).

[4]D. Wang, S. Wu, F. Fu, S. Mai, Y. Yang, Y. Liu, and C. Song, "Mechanisms and characteristics of spatter generation in SLM processing and its effect on the properties," Mater. Des. **117**, 121–130 (2017).

[5]G. Chebil, P. Lapouge, Y. Renollet, C. Davoine, M. Thomas, V. Favier, and M. Schneider, "Study of spatter ejections during laser-powder bed fusion process for aluminum alloys," J. Laser Appl. **33**, 042047 (2021).

[6]C. L. A. Leung, S. Marussi, R. C. Atwood, M. Towrie, P. J. Withers, and P. D. Lee, "In situ X-ray imaging of defect and molten pool dynamics in laser additive manufacturing," Nat. Commun. **9**, 1355 (2018).

[7]N. P. Calta, J. Wang, A. M. Kiss, A. A. Martin, P. J. Depond, G. M. Guss, V. Thampy, A. Y. Fong, J. N. Weker, K. H. Stone, C. J. Tassone, M. J. Kramer,

M. F. Toney, A. Van Buuren, M. J. Matthews, J. Wang, A. M. Kiss, A. A. Martin, P. J. Depond, G. M. Guss, V. Thampy, A. Y. Fong, J. N. Weker, K. H. Stone, C. J. Tassone, M. J. Kramer, M. F. Toney, A. V. Buuren, and M. J. Matthews, "An instrument for *in situ* time-resolved X-ray imaging and diffraction of laser powder bed fusion additive manufacturing processes," Rev. Sci. Instrum. **89**, 055101 (2018).

[8]N. D. Parab, C. Zhao, R. Cunningham, L. I. Escano, K. Fezzaa, W. Everhart, A. D. Rollett, L. Chen, and T. Sun, "Ultrafast X-ray imaging of laser–metal additive manufacturing processes - research papers," J. Synchrotron Radiat. **25**, 1467–1477 (2018).

[9]C. Zhao, K. Fezzaa, R. W. Cunningham, H. Wen, F. De Carlo, L. Chen, A. D. Rollett, and T. Sun, "Real-time monitoring of laser powder bed fusion process using high-speed X-ray imaging and diffraction," Sci. Rep. **7**, 3602 (2017).

[10]H. Ghasemi-Tabasi, C. de Formanoir, S. Van Petegem, J. Jhabvala, S. Hocine, E. Boillat, N. Sohrabi, F. Marone, D. Grolimund, H. Van Swygenhoven, and R. E. Logé, "Direct observation of crack formation mechanisms with *operando* Laser Powder Bed Fusion X-ray imaging," Addit. Manuf. **51**, 102619 (2022).

[11]Q. Guo, C. Zhao, L. I. Escano, Z. Young, L. Xiong, K. Fezzaa, W. Everhart, B. Brown, T. Sun, and L. Chen, "Transient dynamics of powder spattering in laser powder bed fusion additive manufacturing process revealed by in-situ high-speed high-energy x-ray imaging," Acta Mater. **151**, 169–180 (2018).

[12]Q. Guo, C. Zhao, M. Qu, L. Xiong, L. I. Escano, S. M. H. Hojjatzadeh, N. D. Parab, K. Fezzaa, W. Everhart, T. Sun, and L. Chen, "In-situ characterization and quantification of melt pool variation under constant input energy density in laser powder bed fusion additive manufacturing process," Addit. Manuf. **28**, 600–609 (2019).

[13]C. L. A. Leung, S. Marussi, M. Towrie, J. V. Garcia, R. C. Atwood, A. J. Bodey, J. R. Jones, P. J. Withers, and P. D. Lee, "Laser-matter interactions in additive manufacturing of stainless steel SS316L and 13-93 bioactive glass revealed by *in situ* X-ray imaging," Addit. Manuf. **24**, 647–657 (2018).

[14]C. L. A. Leung, S. Marussi, M. Towrie, R. C. Atwood, P. J. Withers, and P. D. Lee, "The effect of powder oxidation on defect formation in laser additive manufacturing," Acta Mater. **166**, 294–305 (2019).

[15]A. A. Martin, N. P. Calta, J. A. Hammons, S. A. Khairallah, M. H. Nielsen, R. M. Shuttlesworth, N. Sinclair, M. J. Matthews, J. R. Jeffries, T. M. Willey, and J. R. I. Lee, "Ultrafast dynamics of laser-metal interactions in additive manufacturing alloys captured by *in situ* X-ray imaging," Mater. Today Adv. **1**, 100002 (2019).

[16]R. Cunningham, C. Zhao, N. Parab, C. Kantzos, J. Pauza, K. Fezzaa, T. Sun, and A. D. Rollett, "Keyhole threshold and morphology in laser melting revealed by ultrahigh-speed x-ray imaging," Science **363**, 849–852 (2019).

[17]S. Hocine, S. Van Petegem, U. Frommherz, G. Tinti, N. Casati, D. Grolimund, and H. Van Swygenhoven, "A miniaturized selective laser melting device for *operando* X-ray diffraction studies," Addit. Manuf. **34**, 101194 (2020).

[18]H. Zheng, Y. Wang, Y. Xie, S. Yang, R. Hou, Y. Ge, L. Lang, S. Gong, and H. Li, "Observation of vapor plume behavior and process stability at single-track and multi-track levels in laser powder bed fusion regime," Metals **11**, 937 (2021).

[19]I. Yadroitsev, A. Gusarov, I. Yadroitsava, and I. Smurov, "Single track formation in selective laser melting of metal powders," J. Mater. Process. Technol. **210**, 1624–1631 (2010).

[20]P. Lhuissier, X. Bataillon, C. Maestre, J. Sijobert, E. Cabrol, P. Bertrand, E. Boller, A. Rack, J.-J. Blandin, L. Salvo, and G. Martin, "In situ 3D X-ray microtomography of laser-based powder-bed fusion (L-PBF)—A feasibility study," Addit. Manuf. **34**, 101271 (2020).

[21]J. J. S. Dilip, S. Zhang, C. Teng, K. Zeng, C. Robinson, D. Pal, and B. Stucker, "Influence of processing parameters on the evolution of melt pool, porosity, and microstructures in Ti-6Al-4V alloy parts fabricated by selective laser melting," Prog. Addit. Manuf. **2**, 157–167 (2017).

[22]G. Kasperovich, J. Haubrich, J. Gussone, and G. Requena, "Correlation between porosity and processing parameters in TiAl6V4 produced by selective laser melting," Mater. Des. **105**, 160–170 (2016).

[23]O. Andreau, E. Pessard, I. Koutiri, J.-D. Penot, C. Dupuy, N. Saintier, and P. Peyre, "A competition between the contour and hatching zones on the high cycle fatigue behaviour of a 316L stainless steel: Analyzed using X-ray computed tomography," Mater. Sci. Eng. A **757**, 146–159 (2019).

[24]M. Tang, P. C. Pistorius, and J. L. Beuth, "Prediction of lack-of-fusion porosity for powder bed fusion," Addit. Manuf. **14**, 39–48 (2017).

[25]G. Mohr, S. J. Altenburg, A. Ulbricht, P. Heinrich, D. Baum, C. Maierhofer, and K. Hilgenberg, "In-situ defect detection in laser powder bed fusion by using thermography and optical tomography—Comparison to computed tomography," Metals **10**, 103 (2020).

[26]T. Vilaro, C. Colin, and J. D. Bartout, "As-fabricated and heat-treated microstructures of the Ti-6Al-4V alloy processed by selective laser melting," Metall. Mater. Trans. A **42**, 3190–3199 (2011).

[27]L. Thijs, F. Verhaeghe, T. Craeghs, J. V. Humbeeck, and J.-P. Kruth, "A study of the microstructural evolution during selective laser melting of Ti–6Al–4V," Acta Mater. **58**, 3303–3312 (2010).

[28]A. Mirone, E. Brun, E. Gouillart, P. Tafforeau, and J. Kieffer, "The PyHST2 hybrid distributed code for high speed tomographic reconstruction with iterative reconstruction and a priori knowledge capabilities," Nucl. Instrum. Methods Phys. Res., Sect. B **324**, 41–48 (2014).

[29]A. Lyckegaard, G. Johnson, and P. Tafforeau, "Correction of ring artifacts in X-ray tomographic images," Int. J. Tomogr. Stat. **18**, 1–9 (2011).

[30]C. A. Schneider, W. S. Rasband, and K. W. Eliceiri, "NIH Image to ImageJ: 25 years of image analysis," Nat. Methods **9**, 671–675 (2012).

[31]V. Boulos, V. Fristot, D. Houzet, L. Salvo, P. Lhuissier, V. Boulos, V. Fristot, D. Houzet, L. Salvo, P. L. Investigating, V. Boulos, V. Fristot, and D. Houzet, "Investigating performance variations of an optimized GPU-ported granulometry algorithm," in *Design and Architectures for Signal and Image Processing (DASIP)* (IEEE, 2012), pp. 1–6.

[32]W. E. King, H. D. Barth, V. M. Castillo, G. F. Gallegos, J. W. Gibbs, D. E. Hahn, C. Kamath, and A. M. Rubenchik, "Observation of keyhole-mode laser melting in laser powder-bed fusion additive manufacturing," J. Mater. Process. Technol. **214**, 2915–2925 (2014).

[33]S. Shrestha, T. Starr, and K. Chou, "A study of keyhole porosity in selective laser melting: Single track scanning with micro-CT analysis," J. Manuf. Sci. Eng. **141**, 071004 (2019).

[34]M. Bayat, A. Thanki, S. Mohanty, A. Witvrouw, S. Yang, J. Thorborg, N. S. Tiedje, and J. H. Hattel, "Keyhole-induced porosities in laser-based powder bed fusion (L-PBF) of Ti6Al4V: High-fidelity modelling and experimental validation," Addit. Manuf. **30**, 100835 (2019).